Dynamic NMR effects in breast cancer dynamic-contrast-enhanced MRI

Xin Li[a], Wei Huang[a,b,c,d], Elizabeth A. Morris[c,d], Luminita A. Tudorica[e,f,g], Venkatraman E. Seshan[h], William D. Rooney[a], Ian Tagge[a], Ya Wang[b], Jingang Xu[a], and Charles S. Springer, Jr.[a,f,i,j,1]

[a]W. M. Keck Foundation High-Field MRI Laboratory–Advanced Imaging Research Center, [f]Knight Cancer Institute, and Departments of [i]Physiology and Pharmacology, [j]Biomedical Engineering, and [g]Radiology, Oregon Health and Science University, Portland, OR 97239; Departments of [b]Medical Physics and [c]Radiology, Memorial Sloan-Kettering Cancer Center, New York, NY 10021; [d]Department of Radiology, Weill Medical College, Cornell University, New York, NY 10021; [e]Department of Radiology, State University of New York, Stony Brook, NY 11794; and [h]Department of Biostatistics, Columbia University, New York, NY 10032

Edited by Alexander Pines, University of California, Berkeley, CA, and approved September 19, 2008 (received for review May 14, 2008)

The passage of a vascular-injected paramagnetic contrast reagent (CR) bolus through a region-of-interest affects tissue ^1H_2O relaxation and thus MR image intensity. For longitudinal relaxation [$R_1 \equiv (T_1)^{-1}$], the CR must have transient molecular interactions with water. Because the CR and water molecules are never uniformly distributed in the histological-scale tissue compartments, the kinetics of equilibrium water compartmental interchange are competitive. In particular, the condition of the equilibrium transcytolemmal water exchange NMR system sorties through different domains as the interstitial CR concentration, [CR_o], waxes and wanes. Before CR, the system is in the fast-exchange-limit (FXL). Very soon after CR_o arrival, it enters the fast-exchange-regime (FXR). Near maximal [CR_o], the system could enter even the slow-exchange-regime (SXR). These conditions are defined herein, and a comprehensive description of how they affect quantitative pharmacokinetic analyses is presented. Data are analyzed from a population of 22 patients initially screened suspicious for breast cancer. After participating in our study, the subjects underwent biopsy/pathology procedures and only 7 (32%) were found to have malignancies. The transient departure from FXL to FXR (and apparently not SXR) is significant in only the malignant tumors, presumably because of angiogenic capillary leakiness. Thus, if accepted, this analysis would have prevented the 68% of the biopsies that proved benign.

water exchange | screening | shutter speed

Nuclear magnetic resonance (NMR) measurements carry information on the dynamics of the signal-producing molecules and/or others interacting with them. This is true whether the NMR sample is a liquid, a solid, or biological tissue. Thus, if correctly analyzed, magnetic resonance imaging (MRI) allows the mapping of molecular dynamic properties.

Quantitative MRI/Dynamic-Contrast-Enhanced MRI (DCE-MRI). Quantitative MRI produces parametric maps of MR, pathophysiological, and/or pharmacokinetic biomarker properties. The DCE-MRI subcategory is particularly significant because it applies to a wide pathology range. In this technique, the T_1-weighted tissue ^1H_2O MRI signal intensity is acquired before, during, and after the (usually) bolus injection of a hydrophilic, paramagnetic contrast reagent (CR) (1). The CR passage through a tissue region-of-interest (ROI) can cause a transient increase of the longitudinal ^1H_2O relaxation rate constant [$R_1 \equiv (T_1)^{-1}$] with consequent elevated MR steady-state signal intensity.

Molecular Imaging of Water. The CR is "detected" indirectly—via its effect on the water proton MR signal (2). Water is the most important biological molecule: Besides its solvent role, it fills the histological-scale tissue compartmental spaces. Water movement between these volumes is crucial in homeostasis and edemic abnormalities. Indeed, one can consider this equilibrium interchange an essential biological activity of water: It is regulated.

However, its very ubiquity makes water molecular MR imaging a challenge. Although the tissue water proton signal is the almost universal MR image source, the unambiguous discrimination of compartmental ^1H_2O resonances—subvoxel (volume element) in origin—is difficult. The use of a CR is almost always required. And, because the CR and H_2O compartmental distributions are always different, the equilibrium intercompartmental water molecule interchange kinetics may become influential and measurable.

Dynamic Nuclear Magnetic Resonance (DNMR). Since almost its beginning, NMR has been recognized as enjoying a unique ability to detect and measure the kinetics of rapid equilibrium (exchange) molecular processes occurring within the sample. In the pre-MRI era, this aspect was commonly referred to as DNMR spectroscopy (3, 4). This terminology follows the deliberate oxymoron, "dynamic equilibrium," of chemistry usage, and thus differs from the (time-dependence) meaning in DCE-MRI. In DNMR, however, the speed of an exchange process is manifest (in signal relaxation exponentiality) only as a heterodyne-like comparison of its intrinsic rate constant with its particular NMR shutter-speed [τ^{-1}] (5) [τ is a generalization of the NMR time-scale (3, 4)]. For the exchange between 2 molecular forms, the spectroscopic τ^{-1} for a nuclear spin is its (intensive) resonance frequency difference ($\Delta\omega$) in the two forms. For tissue ^1H_2O, however, ω is effectively compartment-independent (isochronous).

Just as with DNMR, the neglect of exchange kinetics considerations can lead to systematic errors in parameters extracted by quantitative DCE-MRI analyses. Examples here are the compartmental water mole fractions defining tissue spaces. Therefore, DCE-MRI is also a subcategory of in vivo MR molecular imaging—mapping the distribution and/or activity of molecules in living tissues.

Early in medical MRI development, it was realized that the DCE biomarkers contained considerable information, particularly about vascular properties. Major efforts have been mounted for the pharmacokinetic analyses of DCE time-course data (1). It was natural that mathematical models for these derivations were sought from mature algorithms in the nuclear medicine

Author contributions: W.H., E.A.M., and C.S.S. designed research; W.H., E.A.M., and L.A.T. performed research; X.L., W.H., V.E.S., W.D.R., I.T., Y.W., J.X., and C.S.S. analyzed data; and X.L., W.H., W.D.R., and C.S.S. wrote the paper.

The authors declare no conflict of interest.

This article is a PNAS Direct Submission.

Freely available online through the PNAS open access option.

[1]To whom correspondence should be addressed at: Advanced Imaging Research Center, Oregon Health and Science University, 3181 Southwest Sam Jackson Park Road, Mail Code L452, Portland, OR 97239. E-mail: springer@ohsu.edu.

This article contains supporting information online at www.pnas.org/cgi/content/full/0804224105/DCSupplemental.

field. We refer to such paradigms as members of the standard model (SM) family. However, these formalisms were developed for tracer pharmacokinetics, with the intrinsic feature of direct radiotracer detection. Although the MRI CR plays the tracer role, the signal molecule remains water, which is differently distributed. The direct application of tracer pharmacokinetic models to MRI data (1) resulted in the inadvertent constraint that all intercompartmental equilibrium water exchange be treated as if infinitely fast. This corollary is not valid (2, 6), and its assumption can effectively short circuit MRI determination of CR compartmentalization (2, 7)— the pharmacokinetic essence. In a series of papers (2, 5, 6, 8–16), we have examined the significance of this implication. We refer to models incorporating equilibrium exchange effects in the pharmacokinetic derivation as belonging to the shutter-speed model (SSM) family.

Here, we survey the effects of intercompartmental water exchange kinetics in DCE-MRI breast cancer screening. They appear to facilitate discrimination of benign and malignant lesions, as we show here and in a companion paper (17).

Results

Pharmacokinetic Analyses. Clinical DCE-MRI data are collected in Ernstian NMR steady-states [see *Longitudinal Relaxation Pulse Sequences* in supporting information (SI) *Text*]. An expression for such a tissue ^1H_2O steady-state is given in Eq. **1**,

$$S/S_0 = M/M_0 = \mathbf{S} = p'_i\mathbf{S}_i + p'_o\mathbf{S}_o + p'_b\mathbf{S}_b \qquad [1]$$

where S is the signal intensity and S_0 is that for the sample Boltzmann ^1H_2O magnetization (M_0). The symbols $\mathbf{S}$ are saturation (really *un*saturation) factors (18). Eq. **1** recognizes that each tissue signal comprises potentially separable intracellular, interstitial, and blood compartmental ^1H_2O resonances; subscripts i, o (for outside), and b, respectively. (Plasma and intraerythrocyte blood ^1H_2O signals are averaged under almost all conditions.) The p' coefficients represent the *apparent* water mole fractions (populations) in the physiological compartments of the signal-emanating volume (as small as an image voxel): $p'_i + p'_o + p'_b = 1$. Each $\mathbf{S}$ quantity comprises, in turn, exponential longitudinal and transverse relaxation factors (*Theory* in *SI Text*).

Eq. **1** recognizes that the tissue ^1H_2O signal can potentially exhibit triple-exponential longitudinal relaxation. This possibility is accommodated with a 3×3 exchange matrix accounting for equilibrium water exchange between blood and interstitium and between interstitium and cytoplasm—a 3-site 2-exchange (3S2X) system (2). But it is cumbersome to write nonmatrix algebraic expressions for the *apparent* compartmental quantity (p'_i, $R_1'_i$, p'_o, $R_1'_o$, p'_b, and $R_1'_b$) time-dependencies during CR pharmacokinetic passage in terms of the more fundamental *intrinsic* compartmental properties containing pathophysiological information.

Eliminating the often small blood term (i.e., let $p'_b\mathbf{S}_b \to 0$), on the right-hand side of Eq. **1** leaves a 2-site-exchange (2SX) system, for equilibrium water transcytolemmal interchange. But, nonmatrix algebraic expressions for the p'_i, $R_1'_i$, p'_o, and $R_1'_o$ would still be cumbersome (19). However, there are simpler nonmatrix 2SX equations with *phenomenological* bases. We have presented (18) a version of Eq. **2**,

$$S/S_0 = M/M_0 = \mathbf{S} = a_L\mathbf{S}_L + a_S\mathbf{S}_S \qquad [2]$$

where the notation is that of Eq. **1** except, instead of i and o subscripts, there are L and S subscripts (the primes are unnecessary), which distinguish 2 empirical exponential components with larger and smaller T_1 values, T_{1L} and T_{1S}, respectively (thus, $R_{1S} > R_{1L}$). [The saturation factors are defined: $\mathbf{S}_{L,S} \equiv \{[\sin\alpha(1 - \exp(-TR{\cdot}R_{1L,S}))/(1 - \exp(-TR{\cdot}R_{1L,S})\cos\alpha)]{\cdot}\exp(-TE{\cdot}R^*_{2L,S})\}$, where α is the flip angle, TR and TE are the repetition and echo times, and R^*_2 is the apparent transverse relaxation rate constant.] Ref. 5 provides R_{1L}, R_{1S}, and a_S ($= 1 - a_L$) expressions as functions of p_i, R_{1i}, p_o ($= 1 - p_i$), R_{1o} (the intrinsic values, in the absence of exchange), and τ_i, the mean intracellular water lifetime (reproduced in *Theory* in *SI Text*). [R_{1o} is expressed as ($r_{1o}[CR_o] + R_{1o0}$), where r_{1o} and $[CR_o]$ are the interstitial CR relaxivity and concentration, respectively: R_{1o0} is R_{1o} before CR_o arrival.] The p_i and p_o quantities ($p_i + p_o = 1$) are the true tissue properties of pathophysiological interest—they are measures of the compartmental volume fractions, v_i and v_e, respectively (e for extracellular, extravascular).

After $[CR_o]$ is sufficient, compartmental identifications can be made ($a_L = p'_i$, $R_{1L} = R_1'_i$, $a_S = p'_o$, and $R_{1S} = R_1'_o$). Before $[CR_o]$ becomes very large, it is possible that the S and L compartmental assignments are reversed, because it is possible that $R_{1i} > R_{1o0}$. However, it is not very long at all after CR_o arrival that an assignment switchover occurs (2) to yield the identifications given here, which remain for essentially the entire time CR is present in the tissue.

Before CR_o arrival, τ^{-1} [$\equiv |r_{1o}[CR_o] + R_{1o0} - R_{1i}|$] is effectively zero and sufficiently smaller than the exchange rate constant [$\tau_i^{-1}(1 + (p_i/p_o))$] that the system is in the fast-exchange-limit (FXL) condition. This situation is tantamount to stating that S/S_0 is $\langle p'\mathbf{S}\rangle$ or $\langle a\mathbf{S}\rangle$ on the right-hand sides of Eqs. **1** and **2**, respectively. As CR_o arrives and increases, the system departs the FXL for the fast-exchange-regime (FXR) condition, which we (5) defined to be the situation when the $a_S\mathbf{S}_S$ term on the right-hand side of Eq. **2** (vanished in the FXL) remains negligible. A significant contribution from the $a_S\mathbf{S}_S$ term defines the slow-exchange-regime (SXR) condition (5). As CR_o washes out of the tissue, this progression is reversed. Although cell suspension systems can be driven to the FXR, the SXR, and even the slow-exchange-limit (SXL) (*Exchange Domains* in *SI Text*), there has never been conclusive evidence for a tissue system reaching the SXR in a DCE-MRI study.

We conducted a number of different pharmacokinetic analyses here. The SM assumes that the equilibrium water intercompartmental exchange systems remain in the FXL: it is FXL-constrained (FXL-c). We also used the FXR- and SXR-allowed (FXR-a and SXR-a) versions of the first-generation Shutter-Speed Model (SSM1), BOLus Enhanced Relaxation Overview (BOLERO) (8, 11). In the SM analyses, the parameters varied are K^{trans} and v_e, while the τ_i value is (implicitly) zero (11, 13, 14). [K^{trans} measures the CR extra/intravasation rate (*Theory* in *SI Text*).] In some SSM analyses, τ_i is also varied. The complete 9-parameter set has been tabulated (14) and the constant values of the other parameters have been reported (13, 14).

MRI Data. Data were obtained with consent from patients with positive mammographic and/or clinical MRI reports from standard institutional breast cancer work-ups and protocols. All had MRI contrast-enhanced lesions radiologically classified as Breast Imaging Reporting and Data System (BIRADS) four (B-4, suspicious) or five (B-5, highly suggestive of malignancy) (17). Emphasizing practicability and robustness, the data are of a rather routine clinical nature (they were obtained at 2 different institutions, with 2 different instruments, CRs, etc.): The 2 different data acquisitions were by no means optimized for quantitative DCE-MRI. For example, the pulse sequence parameters were prescribed by radiological spatial resolution and tissue volume coverage considerations because many images were to be used to guide immediately subsequent surgical interventions. The pharmacokinetic period is truncated, and although the spatial resolution is reasonable, the temporal resolution is not optimal. Also, the adipose tissue $-^1H_2C-$ MR signal is suppressed in only one institution's acquisitions.

Fig. 1*A* shows the 3.3-min pharmacokinetic image of sagittal

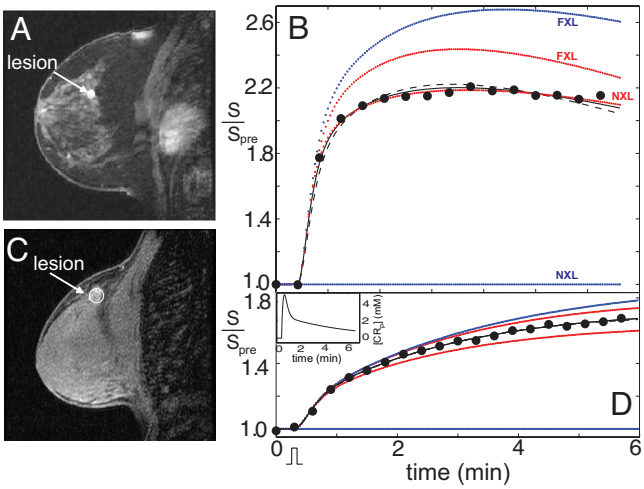

Fig. 1. Sagittal, fat-suppressed breast DCE-MRI image planes containing a malignant invasive and in situ ductal carcinoma (IDC/DCIS) (*A*) and a benign lobular carcinoma in situ with stromal fibrosis (*C*) are shown. The relative ^1H_2O signal (S/S_{pre}) DCE-MRI time courses (circles) for ROIs containing the malignant and benign lesions are shown in *B* and *D*, respectively. The arterial input function (the plasma CR concentration variation) used in the analyses is shown in the *Inset* in *D*. There are 3 model-fitted (black) curves associated with each lesion data set. The dashed curves represent the best fittings with the SM (FXL-c). The solid curves represent the best fittings with the FXR- and the SXR-a SSM versions. [All are indistinguishable except for the dashed fitting to the IDC/DCIS data (*B*).] The model parametric values of these fittings are given in Table 1. The dotted curves represent the exchange-limiting expectations with the SSM parametric values. The upper curves delimit the FXL conditions, whereas the lower curves delimit the NXL conditions—red and blue for the SXR-a and FXR-a SSM analyses, respectively.

slice 20 (from lateral to medial) of a 57-year-old subject's left breast [patient 4 (17)]. The ROI marked represents 17 pixels (10 mm^2, 31 μL) containing the tiny lesion evident in this slice, subsequently found to contain both malignant invasive and in situ ductal carcinoma (IDC/DCIS). Fig. 1*C* shows the 3.6-min pharmacokinetic image of slice 12 of a 52-year-old subject's left breast [patient 8 (17)]. The ROI there represents 164 pixels (81 mm^2, 243 μL) containing the lesion evident in this slice, subsequently found to comprise benign lobular carcinoma in situ and stromal fibrosis (LCIS/SF). These images were acquired with adipose –^1H_2C– suppression (institutional protocol required). In contrast to those (13, 14) obtained with no fat suppression, these darker images show glandular regions brighter than fatty tissues.

The ^1H_2O S/S_{pre} time courses for these 2 ROIs are shown in Fig. 1 *B* and *D* (circles). The CR injection timing is suggested by the rectangular function below the Fig. 1*D* abscissa. The shape of the IDC/DCIS ROI data (Fig. 1*B*) is that often reported as characteristic of such tumors: much faster and greater uptake (followed by washout) compared with a benign lesion such as that of Fig. 1*D* (13, 20–23). The mean arterial input function (AIF), determined from axillary artery ^1H_2O signal time courses in 3 patients, shows the plasma CR concentration, $[CR_p]$, peaking near 5 mM at ≈0.75 min (Fig. 1*D Inset*).

There are many traces in Fig. 1 *B* and *D*. Three curves each are fitted to the IDC/DCIS ROI data and the LCIS/SF ROI data. The black dashed curve distinguishable in Fig. 1*B* represents the best FXL-c (SM) fitting of the data. The model has the constraints that τ_i is vanishingly small (the FXL) and that the transverse relaxation factor $[\exp(-TE{\cdot}R_2^*)] = 1$. The dashed curve shows the characteristic undershoot at the beginning, followed by overshoot and then undershoot during the washout (11, 13, 14). The K^{trans} and v_e parameter values from this fitting are listed in Table 1. [Other parameter relationships and fixed values are given in the table legend. Acquisition pulse sequence parameter values (*Materials and Methods*) were also used.] The black solid curves represent the fittings from the FXR-a and SXR-a versions of SSM, which are equally better than the FXL fitting and are thus superimposed. These fittings employ the constraints that τ_i is held fixed at 0.4 s (the reason for this value will be seen below) and that (especially for SXR-a) $\exp(-TE{\cdot}R_{2L,S}^*)$ are each = 1. The latter are of course not necessarily true (see below). The FXR-a version has the additional constraint to only the Eq. **2** $\mathbf{S}_L$ factor ($a_L \to 1$, $a_S \to 0$). Except for the FXL-c (SM) analysis of IDC/DCIS, the *random* fitting errors ($\chi^2\sigma^2$, given and defined in Table 1) are not widely different. Of course the FXR-a and SXR-a fittings return K^{trans} and v_e values different from FXL-c (Table 1): The v_e values are increased, as is K^{trans} for the FXR-a IDC/DCIS fitting. All 3 fitted curves are essentially superimposed for the Fig. 1*D* LCIS/SF data.

Normal-appearing glandular (NAG) or adipose tissue ROI signal time courses show almost no enhancement (see figures 1b and d of ref. 13 and 1c of ref. 14). Fittings of NAG data typically yield very small parameter values; $K^{trans} = 0.0004$ min^{-1} and $v_e = 0.03$.

There are 4 additional dotted curves (blue and red pairs) each in Fig. 1 *B* and *D*. The top member of each pair represents the FXL ($\tau_i \to 0$) expectation for the FXR-a (blue) and for the SXR-a (red) Table 1 parameter values. The bottom members represent the corresponding no-exchange-limit (NXL) ($\tau_i \to \infty$) expectations. Thus, the vertical dynamic range between the top and bottom members of a pair is a measure of the model exchange sensitivity for this acquisition of these data. This property is not the same as the shutter-speed. The τ^{-1} variation during the CR bolus passage, in comparison with the constant exchange rate constant $[\tau_i^{-1}(1 + (p_i/p_o))]$, determines the position of the data within the exchange sensitivity range.

We have reported other examples of the top blue curves; see figures 1d of ref. 14 and 1b and d of ref. 13. Note the significantly

Table 1. Fitting results for Fig. 1

	FXL-c (SM)			FXR-a (SSM)			SXR-a (SSM)		
Lesion	K^{trans}, min^{-1}	v_e	τ_i, s	K^{trans}, min^{-1}	v_e	τ_i, s	K^{trans}, min^{-1}	v_e	τ_i, s
IDC/DCIS (Fig. 1 *A* and *B*) patient 4	0.153 (± 0.014)	0.29 (± 0.03)	→ 0	0.211 (± 0.017)	0.64 (± 0.06)	0.40 (fixed)	0.155 (± 0.008)	0.38 (± 0.01)	0.40 (fixed)
$\chi^2\sigma^2$		0.14			0.018			0.0085	
LCIS/SF (Fig. 1 *C* and *D*) patient 8	0.032 (± 0.003)	0.27 (± 0.07)	→ 0	0.033 (± 0.004)	0.63 (± 0.07)	0.40 (fixed)	0.026 (± 0.001)	0.42 (± 0.07)	0.40 (fixed)
$\chi^2\sigma^2$		0.0037			0.0036			0.0017	

Other parameter relationships and fixed values: r_{1o} (fixed at 4.1 $s^{-1}{\cdot}mM^{-1}$); $v_e = f_W(1 - p_i)$, where f_W is the volume fraction accessible to mobile aqueous solutes (fixed at 0.8); $R_{1o0} = (R_{10} - p_iR_{1i})/(1 - p_i)$, where R_{10} is the tissue ^1H_2O R_1 before CR arrival (fixed at 0.55 s^{-1}); R_{1i} (fixed at 0.55 s^{-1}); $[CR_b] = (1 - h_s)[CR_p]$, where h_s is the microvascular hematocrit (fixed at 0.3) (17). Fitting errors: χ^2 is a weighted sum of squared residuals, and σ is the standard deviation at each time point [Yankeelov TE, *et al.* (2005) Evidence for shutter-speed variation in CR bolus-tracking studies of human pathology. *NMR Biomed* 18:173–185].

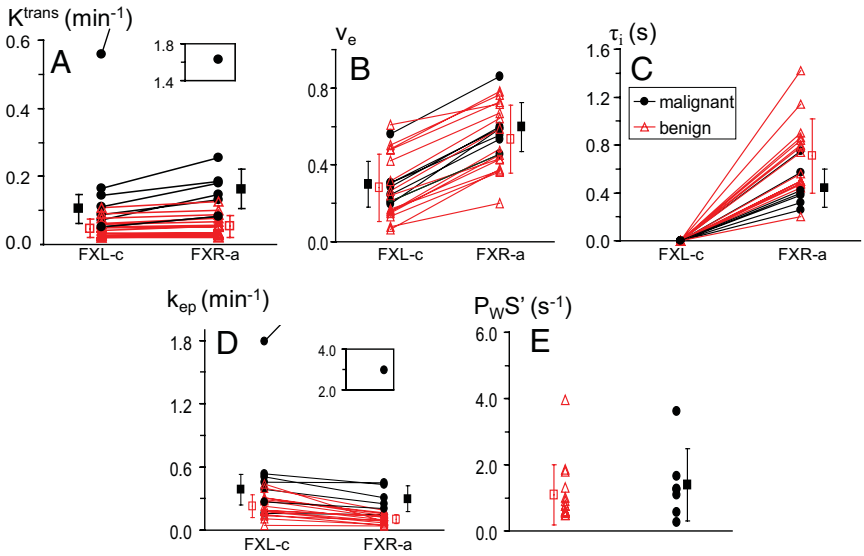

Fig. 2. Scatter plots show the DCE-MRI pharmacokinetic parameter values for 22 subject lesion ROIs. Black circles represent those proven malignant by subsequent biopsy/pathology, whereas red triangles indicate those found solely benign. *A–C* give the 3 traditional independent parameter (K^{trans}, v_e, and τ_i) values, respectively measuring the CR extravasation rate, the interstitial volume fraction, and the mean intracellular water lifetime. Precise definitions are given in the text. *D* and *E* give the analogous plots of the linear combination K^{trans}/v_e and $(1 - v_e)/\tau_i$ parameters, which respectively measure k_{ep} (the CR intravasation rate constant) and the cytolemmal water permeability coefficient surface area product (P_WS'). For *A–D*, the left column gives the SM (FXL-c) results, and the right column gives the SSM (FXR-a) results. Connector lines join individual ROI values. Because the SM considers P_WS' infinitely large, *E* shows only the SSM results. The group mean values are given as squares on the left and right sides for the SM and SSM columns, respectively. The error bars represent (±SD) values within each category. One malignant lesion FXR-a column outlier is plotted in the *Insets* in *A* and *D* and is excluded from the SD calculations for both the FXL-c and FXR-a results in those panels.

greater difference between the top blue curve and the data for the malignant IDC/DCIS (Fig. 1*B*) than for the benign LCIS/SF (Fig. 1*D*) tumor. This mismatch was also seen in the comparison of an IDC with a benign fibroadenoma (figure 1b and d of ref. 13). This observation is a preview of the FXR-a analysis ability to discriminate malignant from benign breast tumors. The only way the FXL-c (SM) model can bring the blue dotted curve down to the data circles is by reducing parameter values below those for the FXR-a fitting. Although the SM comes close to matching the data for the benign lesion, it fails much more significantly for the malignant tumor—just when needed.

The NXL expectation for the FXR-a parameters (bottom blue dotted line) shows no S/S_{pre} change during the CR bolus passage. For the NXL, $a_S \rightarrow (1 - p_i)$, $R_{1S} \rightarrow r_{1o}[CR_o] + R_{1o0}$, $a_L \rightarrow p_i$, and $R_{1L} \rightarrow R_{1i}$, as they must ($R_{1S} > R_{1L}$). Thus, in this limit, $R_{1L} = R_{1i}$, which is $[CR_o]$-independent, and because there is only $\mathbf{S}_L$ for the FXR-a Eq. **2** version, S is constant. The exchange sensitivity for analysis by the FXR-a version (blue curves) is necessarily greater than that for analysis of the same data by the SXR-a version (red curves). One way to understand this maxim is by inspecting theoretical putative calibration curves implicit in the analyses [*Calibration Curves* in *SI Text*]. Before CR_o arrival, a_S is zero and R_{1L} is $p_iR_{1i} + p_oR_{1o}$: the FXL. When CR_o first arrives, a_S grows only very slowly: the FXR condition obtains until its contribution becomes significant (5, 18).

However, it is very interesting that the Fig. 1*B* IDC/DCIS data are essentially superimposed on the no-exchange limiting (bottom red) curve for the SXR-a model. [We have obtained a similar result for transendothelial water exchange (16).] Consistently, if these data are analyzed with the SXR-a model floating τ_i, it returns the algorithm's upper bound value. We stopped when τ_i exceeded the unrealistically large 35 s. This behavior is true for 6 of the 7 malignant tumors in this population. In contrast, the Fig. 1*D* benign LCIS/SF data are clearly inside the smaller red dotted curve exchange range. Correspondingly, the SXR-a fitting with floating τ_i returned a value of 110 ms. However, most of the benign lesions (11 of the 15 total) exhibited the same upper bound indeterminacy as the malignant tumor in this regard.

The FXR-a calibration curves (*SI Text*) imply that there will be greater parameter value differences between FXL-c (SM) and FXR-a (SSM) analyses. This result is seen in Table 1. For the IDC/DCIS data, FXR-a analysis increases v_e by more than 2-fold and K^{trans} by 38%. If τ_i is let float, FXR-a analysis returns a value of 360 (± 58) ms (SD) (with no K^{trans} change and an 8% v_e decrease), which is very reasonable (as we will see below).

Ostensibly, the SXR-a model includes the FXR-a model. However, the results suggest that the SXR-a model is less compatible with the data, an indication of systematic error. We will discuss possible reasons for this below. We now present the results for analyses of the data from all of the lesions by using the FXL-c SM and the FXR-a SSM. As we will see, these breast screening DCE-MRI data seem quite compatible with FXR-a analyses.

Comparison of Pharmacokinetic Model and Gold Standard Pathology Analyses. For each of the 22 patients, 2 investigators independently analyzed ROI data from 1 sagittal image slice (of 16 to 40 per breast) exhibiting a lesion biopsied only post-DCE. They were each blinded to the biopsy pathology reports. An ROI boundary was independently manually drawn around the entire lesion in a pharmacokinetic image showing near maximal enhancement. The results of 2 different pharmacokinetic analyses (FXL-c and FXR-a) of the DCE-MRI data from the 22 lesion ROIs by each investigator were then averaged lesion-by-lesion, model-by-model, and parameter-by-parameter. The FXL-c analyses varied K^{trans} and v_e, whereas the FXR-a analyses also varied τ_i. Fig. 2 presents 1D scatter plots in each of 5 different single parametric space dimensions: K^{trans} (*A*), v_e (*B*), τ_i (*C*), K^{trans}/v_e (*D*), and $(1 - v_e)/\tau_i$ (*E*). The latter two are pair-wise linear combinations from the first 3 traditional adjustable model parameters; their definitions are elaborated below. In each case,

the 7 proven malignant lesion ROI results are shown as black circles, with the 15 solely benign lesion ROI results as red triangles. Subsequent biopsy and pathology analyses proved 15 (13 of the 17 B-4 and 2 of the 5 B-5) lesions to be of several different solely benign types. The (only) 7 (4 B-4 and 3 B-5) malignant lesions comprised 3 IDCs, 1 DCIS, and 2 IDC/DCIS and 1 IDC/LCIS mixtures. The companion paper (17) provides details.

For each parametric dimension [except $(1 - v_e)/\tau_i$] (Fig. 2*E*), the left and right columns represent the results of the SM (FXL-c) and SSM (FXR-a) analyses, respectively. The SM/SSM pair representing each ROI has a connector line. The group mean values for each parameter are given as squares on the left and right sides for the SM and SSM analyses, respectively. The error bars represent SD values within each category. There is one malignant (B-5) outlier so elevated that it is plotted in Fig. 2 *A* and *D* FXR-a column insets and is excluded from the Fig. 2 *A* and *D* SD calculations.

It is obvious that none of the SM parameters allows complete separation of the circles (malignant) and triangles (benign). None achieve anywhere near 100% positive predictive value (PPV) (the best is 54%, for SM K^{trans}). Compared with the SSM, the SM generally underestimates the parameter value [albeit with some precision benefit from reduced parametrization (11, 14)], except for k_{ep} (Fig. 2*D*) and $(1 - v_e)/\tau_i$ (Fig. 2*E*). The latter is effectively infinite in the SM. *Discussion* arguments suggest that these underestimations are in the absolute sense. Importantly, in the K^{trans} and K^{trans}/v_e (Fig. 2 *A* and *D*) cases, it is the SM misestimation that prevents better separation of circles and triangles achieved by the SSM (70% PPV for each). For the K^{trans} parameter (Fig. 2*A*), the SM underestimation has occurred in *only malignant* tumor ROIs (circles). [These include the Fig. 1 malignant/benign ROI pair (Table 1), and the only other such pair reported (13).] One black circle is comingled with the red triangles in the Fig. 2*A* SSM column only because of partial volume dilution (17). For K^{trans}/v_e (Fig. 2*D*), it is the SM overestimation of particularly benign ROI values that prevents their almost complete separation achieved by the SSM. [The ratio K^{trans}/v_e is equal to k_{ep}, the unidirectional CR intravasation rate constant. For passive CR transport, k_{ep} is equal to $(v_b/v_e)k_{pe}$ (1); v_b is the tissue blood volume fraction, and k_{pe} is the rate constant for CR extravasation.] These K^{trans} and k_{ep} parameter behaviors are not observed for the SXR-a analyses.

There are several other items of note in Fig. 2. The SSM v_e values are increased in both benign and malignant lesions, and they rise to be quite large in some cases, all but one of them benign (Fig. 2*B*). The large v_e malignant tumor is mostly benign (17). Although the malignant and benign τ_i values become finite [and quite reasonable (see below)] with the SSM analyses (Fig. 2*C*), they overlap considerably (thus, this behavior does not contribute to discrimination). It is interesting that the benign values tend to be somewhat larger, although less certain. Although τ_i^{-1} is proportional to the mean *individual* cellular claustrophobic ratio [surface area (A) to volume (V)] (6), it also increases with the transcytolemmal water permeability coefficient [$\tau_i^{-1} = P_W(A/V)$]. The P_W magnitude can reflect the extent of cytolemmal aquaporin expression and/or the cellular metabolic status. The ratio $(1 - v_e)/\tau_i \approx (1 - v_e - v_b)/\tau_i = v_i/\tau_i = P_W S'$, where v_i is the tissue intracellular volume fraction and S' is the *total* cell surface area per voxel volume. $P_W S'$ is considered infinitely large by the SM. When $P_W S'$ is calculated by the SSM, the benign tumor values cluster considerably around 1.1 s^{-1} and the malignant tumors around 1.3 s^{-1} (Fig. 2*E*). Even more remarkable clustering is seen for the SSM benign k_{ep} values, near 0.15 min^{-1} (Fig. 2*D*). This finding reinforces the common notion of considerably greater heterogeneity in malignant tumors. It also means that, although the SSM v_e values show considerable scatter (and no discriminatory power) (Fig. 2*B*), they are well correlated with the SSM K^{trans} values; see the companion paper (17).

Discussion

The Fig. 2*A* results are particularly interesting. For the 15 benign lesions, there is essentially no change in K^{trans} between the SSM (FXR-a) and SM (FXL-c) analyses [in most cases, there is absolutely no change (within error)]. However, in every one of the 7 malignant tumors, there is a K^{trans} decrease upon going to the SM analysis. Because malignant breast tumors are angiogenic (21, 24), it is sensible that malignant lesions have larger K^{trans} values. This inference suggests that the greater overlap of the FXL-c (SM) benign/malignant K^{trans} values represents underestimations in the malignant cases: The K^{trans} values are actually different. The mean ΔK^{trans} [$\equiv K^{trans}$(FXR-a) − K^{trans}(FXL-c)] is 0.06 min^{-1} for 6 malignant tumors and 0.006 min^{-1} for the 15 benign lesions (17). This biomarker allows their complete discrimination (100% PPV) (17). This result and other Fig. 2 entries suggest that the FXR-a analyses are yielding reasonable results in the absolute sense. Although with varying precision, the parameter values determined agree quite well with independent measures (*Literature Comparison* in *SI Text*).

It is particularly the τ_i aspects of applying the SXR-a SSM version to the malignant tumor data that suggest SXR-a incompatibility. As stated above, for 86% of the malignant tumor and 73% of the benign lesion ROIs, SXR-a analyses floating τ_i increased its value until the program incrementation limit was reached. In most cases, the upper bound allowed was 40 s. Fig. 1*B* shows that the IDC/DCIS data points are on the (red) NXL curve for the SXR-a model. As far as SXR-a analyses are concerned, $\tau_i \rightarrow \infty$ for these breast tumors. This extreme is unreasonable and cannot be attributed to only τ_i uncertainty.

Thus, the cumulative weight of the literature results cited and our own results suggests that the FXR-a analyses yield reasonable pharmacokinetic parameter values when the SXR-a analyses do not. Why might that be?

One possibility is that none of the many diverse biological systems studied in the literature proceed sufficiently to depart the FXR for the SXR. However, if so, SXR-a analyses would give the same results as FXR-a analyses, because the former differs only if the SXR condition is reached.

A second possibility lies in the way the FXR-a analyses are performed. At each pharmacokinetic time point, the (extensive) signal intensity is used to estimate the (intensive) R_{1L} value—because there is only the $\mathbf{S}_L$ factor on the right-hand side of Eq. **2**. Then, it is the R_{1L} time-dependence that is fitted. This operation may effectively unweight any contribution from an actual $a_S\mathbf{S}_S$ term. Because there is only a single recovery time point (at TR), this seems a particularly parsimonious approach.

A third possibility is that the SXR-a analyses overestimate the $\mathbf{S}_S$ factor contribution, which could be *disproportionately* quenched by transverse relaxation. The $a_S\mathbf{S}_S$ term always begins at zero and grows only slowly with increasing $[CR_o]$ (*Calibration Curves* in *SI Text* and Fig. S1). The fractional $a_S\mathbf{S}_S$ contribution transiently maximizes (at $[CR_o]_{max}$) at ≈0.05 and ≈0.29 for benign and malignant tumors, respectively, even with $\exp(-TE{\cdot}R^*_{2S}) = 1$. It is much smaller for most of the time course. Surely, however, the $\exp(-TE{\cdot}R^*_{2L,S})$ factors are not actually unity for real acquisitions. Although still mostly intravascular, paramagnetic CR causes significant magnetic field inhomogeneities in perivascular spaces. As $[CR_o]$ rises from zero, the first populations of interstitial water molecules whose magnetization distinguishes itself as a_S are those furthest from cells; some is pericapillary water. Then, as $[CR_o]$ increases further, the increasing interstitial/cytoplasmic magnetic susceptibility difference leads to increasing field inhomogeneities in the entire interstitium. These aspects cause tissue R^*_{2S} to become significantly greater than R^*_{2L}. Even with the small TE of 3.5 ms, $\exp(-TE{\cdot}R^*_{2S})$ would be reduced to 0.57 if R^*_{2S} increased to only 160 s^{-1}. For a homogeneous Lorentzian spectral line, this rate

constant corresponds to a width at half maximum, $\Delta\nu_{1/2}$ [$\equiv R^*_{2S}/\pi$] of 51 Hz, which at 1.5 T is only 0.8 ppm. This linewidth is easily possible (*Interstitial Field Inhomogeneities* in *SI Text*). Thus, it may very well be that $a_S\mathbf{S}_S\{\equiv a_S[\sin\alpha(1-\exp(-TR\cdot R_{1S}))/(1-\exp(-TR\cdot R_{1S})\cos\alpha)]\cdot\exp(-TE\cdot R^*_{2S})\}$ is always significantly quenched [<0.17 ($=0.29\cdot0.57$)] below the SXR-a expectation. At any rate, the FXR range is likely extended to a larger [CR_o] value. The data behave as if they have been edited for $\mathbf{S}_L$: the dominant intensive R_{1L} property may be somewhat immune to variations of the extensive a_L and a_S properties.

Conclusions

The DCE-MRI acquisitions for these data, prescribed for radiological considerations, were not particularly exchange sensitive. Even so, exchange effects seem to facilitate very high discrimination of malignant from benign breast tumors (17). In recent years, there has been considerable effort devoted to decreasing DCE-MRI pulse sequence exchange sensitivity (25). Our results suggest that there could be significant profit, not the least for cancer screening, in working to *increase* exchange sensitivity, by adjusting not only α and TR, but also TE (a small increase may improve specificity). The considerations expressed here could guide such endeavors.

Materials and Methods

Details on some of the MRI data acquisitions and analyses have been published (13, 14); more particulars and differences are presented here.

Patients. Twenty-two patients were recruited from clinical breast cancer populations that had undergone initial screening (mammographic and/or clinical breast MRI protocols) at 2 different institutions: Stony Brook (SB) and Sloan-Kettering (SK). All were placed in the B-4 ($n = 17$) or B-5 ($n = 5$) classifications, which were to lead to biopsy procedures. Numerous details on the subjects are given in the companion paper (17).

DCE-MRI Data Acquisition. The study was conducted using 2 different 1.5-T MR systems [Edge (Philips/Marconi), SB; Excite (General Electric), SK] with body radiofrequency transmit coils, and 4- (SB and SK) and 7-channel (SK) phased-array, prone patient, bilateral breast radiofrequency receive coils having compression plates. A 3D SPGR pulse sequence was used to acquire 12–20 serial sagittal image volume sets continually, covering the entire breast with the suspicious lesion to be biopsied. Other parameters included 10° (SK) and 30° flip angles, 3- to 4-ms TE, 6- to 9-ms TR, 3-mm section thickness, 18- to 24-cm field of view, and 256 × 128 and 256 × 64 (SB) matrix sizes, zero-filled to 256 × 256 during image reconstruction. The SK acquisitions suppressed the fat $-^1H_2C-$ signal with narrow-band saturation radiofrequency pulses centered on its ω value. The phase-encoding direction was superior/inferior. Depending on the breast size, each volume set contained 16–32 image sections, resulting in 13- to 28-s temporal resolutions. At the start of the second volume set acquisition, the CR [gadolinium diethylenetriamine pentaacetate bismethylamide (GdDTPA-BMA) (Omniscan; Nycomed), SB; $GdDTPA^{2-}$ (Magnevist; Berlex), SK] was delivered via an antecubital vein (0.1 mmol/kg at 2 mL/s) and followed by a saline flush, using programmable power injectors (Spectris; Medrad).

DCE-MRI Pharmacokinetic Analyses. An ROI was manually drawn within an axillary artery visible in 3D volume image slices. This region was used for AIF determination. For each of the 6 SB patients, the representative AIF from one of them was used. This trace is shown in figures 1 of refs. 13 and 14. Individual AIF time courses were measured for 3 different SK patients. A mean AIF time course (Fig. 1*D Inset*) was generated by simply averaging these trajectories and used for each of the 16 SK subjects. These AIF time-course data were interpolated by using a 7-parameter empirical expression (11). For each patient, an ROI was manually drawn to circumscribe the entire enhanced lesion in a DCE-MRI image exhibiting near maximal enhancement. The mean tumor tissue ^1H_2O ROI DCE signal intensity/AIF time-course pairs were then subjected to both SM (FXL-c) and SSM (FXR-a) pharmacokinetic analyses to extract K^{trans}, v_e, and τ_i (SSM only) parameter values. Many details of the SM and SSM pharmacokinetic modeling of time-course data are described above, and some images from the 6 SB subjects (3 malignant and 3 benign tumors) have been reported (13, 14).

ACKNOWLEDGMENTS. We thank Drs. J. Evelhoch for SI ref. 32; M. Jerosch-Herold, T. Barbara, and M. Pike for important discussions; Messrs. C. Nyman and T. Mair for technical assistance; and Drs. A. Khilnani, R. Wynn, S. Brennan, and J. Kaplan for recruitment of patients. This work was supported by National Institutes of Health Grants R01 NS-40801, EB-00422 (to C.S.S.) and CA-120861 (to W.H.), the W. M. Keck Foundation (C.S.S.), a Stony Brook University–Brookhaven National Laboratory Seed Grant (to W.H. and C.S.S.), and a Memorial Sloan-Kettering Cancer Center Byrne Fund award (to W.H.).

1. Tofts PS, *et al.* (1999) Estimating kinetic parameters from dynamic contrast-enhanced T_1-weighted MRI of a diffusable tracer: Standardized quantities and symbols. *J Magn Reson Imaging* 10:223–232.
2. Li X, Rooney WD, Springer CS (2005) A unified magnetic resonance imaging pharmacokinetic theory: Intravascular and extracellular contrast reagents. *Magn Reson Med* 54:1351–1359, and erratum (2006) 55:1217.
3. Tanny SR, Pickering M, Springer CS (1973) Increasing the time resolution of dynamic nuclear magnetic resonance spectroscopy through the use of lanthanide shift reagents. *J Am Chem Soc* 95:6227–6232.
4. Bryant RG (1983) The NMR time scale. *J Chem Ed* 60:933–935.
5. Landis CS, *et al.* (1999) Equilibrium transcytolemmal water-exchange kinetics in skeletal muscle *in vivo*. *Magn Reson Med* 42:467–478.
6. Labadie C, Lee J-H, Vétek G, Springer CS (1994) Relaxographic imaging. *J Magn Reson B* 105:99–112.
7. Donahue KM, Weisskoff RM, Burstein D (1997) Water diffusion and exchange as they influence contrast enhancement. *J Magn Reson Imaging* 7:102–110.
8. Landis CS, *et al.* (2000) Determination of the MRI contrast agent concentration time course *in vivo* following bolus injection: Effect of equilibrium transcytolemmal water exchange. *Magn Reson Med* 44:563–574.
9. Springer CS, Rooney WD, Li X (2002) The effects of equilibrium transcytolemmal water exchange on the determination of contrast reagent concentration *in vivo*. *Magn Reson Med* 47:422–424.
10. Quirk JD, *et al.* (2003) Equilibrium water exchange between the intra- and extracellular spaces of mammalian brain. *Magn Reson Med* 50:493–499.
11. Yankeelov TE, Rooney WD, Li X, Springer CS (2003) Variation of the relaxographic "shutter-speed" for transcytolemmal water exchange affects the CR bolus-tracking curve shape. *Magn Reson Med* 50:1151–1169.
12. Zhou R, Pickup S, Yankeelov TE, Springer CS, Glickson JD (2004) Simultaneous measurement of arterial input function and tumor pharmacokinetics in mice by dynamic contrast enhanced imaging: Effects of transcytolemmal water exchange. *Magn Reson Med* 52:248–257.
13. Li X, *et al.* (2005) Shutter-speed analysis of contrast reagent bolus-tracking data: Preliminary observations in benign and malignant breast disease. *Magn Reson Med* 53:724–729.
14. Yankeelov TE, *et al.* (2005) Evidence for shutter-speed variation in CR bolus-tracking studies of human pathology. *NMR Biomed* 18:173–185.
15. Chang EY, *et al.* (2008) The evaluation of esophageal adenocarcinoma using dynamic contrast enhanced magnetic resonance imaging. *J Gastrointestinal Surg* 12:166–175.
16. Li X, Springer CS, Jerosch-Herold M (2008) First-pass DCE-MRI with extravasating CR: Evidence for human myocardial capillary recruitment in adenosine-induced hyperemia. *NMR Biomed*, 10.1002/nbm.1293.
17. Huang W, *et al.* (2008) The MR shutter-speed discriminates vascular properties of malignant and benign breast tumors *in vivo*. *Proc Natl Acad Sci USA*, 10.1073/PNAS.0711226105.
18. Springer CS, Yankeelov TE, Li X, Rooney WD, Medina DC (2004) Longitudinal relaxographic NMR "shutter-speed" for equilibrium transcytolemmal water exchange varies with interstitial CR level. *Proc Int Soc Magn Reson Med* 12:1969.
19. Horská A, Horský J, Spencer RGS (1994) Measurement of spin-lattice relaxation times in systems undergoing chemical exchange. *J Magn Reson A* 110:82–89.
20. Tofts PS, Berkowitz B, Schnall MD (1995) Quantitative analysis of dynamic Gd-DTPA enhancement in breast tumors using a permeability model. *Magn Reson Med* 33:564–568.
21. Buadu LD, *et al.* (1996) Breast lesions: Correlation of the contrast medium enhancement patterns on MR images with histopathologic findings and tumor angiogenesis. *Radiology* 200:639–649.
22. Degani H, Gusis V, Weinstein D, Fields S, Strano S (1997) Mapping pathophysiological features of breast tumors by MRI at high spatial resolution. *Nat Med* 3:780–782.
23. Daniel BL, *et al.* (1998) Breast disease: Dynamic spiral MR imaging. *Radiology* 209:499–509.
24. Salter JT, Miller KD (2007) Antiangiogenic agents in breast cancer. *Cancer Invest* 25:518–526.
25. Kim YR, Rebro KJ, Schmainda KM (2002) Water exchange and inflow affect the accuracy of T_1-GRE blood volume measurements: Implications for the evaluation of tumor angiogenesis. *Magn Reson Med* 47:1110–1120.

Supporting Information

Li *et al.* 10.1073/pnas.0804224105 10.1073/pnas.0804224105

SI Text

Longitudinal Relaxation Pulse Sequences. As with pharmacokinetic analyses, the radiofrequency and gradient pulse sequences for DCE-MRI data acquisition can be divided into two general families. Those attempting actual ^1H_2O R_1 value evaluation during its CR pharmacokinetic variation can be deemed of the Quantitative T_1 family (1, 2). Unlike classic inversion- or saturation-recovery (IR, SR) acquisitions, some attempt "reading" magnetization even during a nominal single longitudinal relaxation period (1, 3, 4) Nonetheless, they still tend to require significant sampling times, and thereby limit pharmacokinetic spatiotemporal resolution and/or the volume coverage of the tissue of interest.

The other acquisition family features radiofrequency and gradient pulse trains establishing "Ernstian" MR steady-states and acquisitions that monitor the pharmacokinetic variation of these. We call this the Steady-State family. Its members can feature quite small sampling times, yielding good spatiotemporal resolution and/or volume coverage.

Although there has been a significant evolution of increasingly efficient Quantitative T_1 sequences (5), these are rarely used for clinically-oriented human DCE-MRI studies, where sampling time constraints are severe. For the latter, MR Steady-State acquisitions are almost universally used. A very common example, and that used here, is the SPGR (SPoiled Gradient-Recalled) sequence. Since only a single TR value is used in these, it is not possible to tell directly whether the ^1H_2O signal at any particular time in the DCE-MRI time-course has 2 or 3 longitudinal relaxation exponential components (Eqs. **1**, **2**, **S1**, **S2**).

Theory. The magnetization saturation factors of Eq. **1** in the main text are expressed in Eq. **S1**.

$$\mathbf{S}_{i,o,b} = f\{[\sin\alpha(1 - E_1{}'_{i,o,b})/(1 - E_1{}'_{i,o,b}\cos\alpha)],\ E^*_{2\,i,o,b}\} \qquad \textbf{[S1]}$$

The subscripts 1 and 2 designate longitudinal and transverse relaxation, respectively, and the E factors are defined in Eqs. **S2** and **S3**.

$$E_1{}'_{i,o,b} = \exp(-TR\cdot R_1{}'_{i,o,b}) \qquad \textbf{[S2]}$$

$$E^*_{2\,i,o,b} = \exp(-TE\cdot R^*_{2\,i,o,b}) \qquad \textbf{[S3]}$$

The prime and * superscripts represent the *apparent* compartmental ^1H_2O relaxation rate constants. The quantities α, TR, and TE are the sequence read pulse flip angle, repetition, and echo times, respectively.

The Bloch longitudinal NMR relaxation rate law was modified for isochronous 2-site-exchange by Woessner (6), and we (7) expressed this for the R_{1L}, R_{1S}, and a_S quantities of Eq. **2** of the main text. They are reproduced here in Eqs. **S4**–**S6**.

$$R_{lL} = \frac{1}{2}\left[R_{li} + r_{lo}[CR_o] + R_{lo0} + \tau_i^{-1} + \frac{p_i}{\tau_i(1-p_i)}\right] - \frac{1}{2}\left\{\left[R_{li} - r_{lo}[CR_o] - R_{lo0} + \tau_i^{-1} - \frac{p_i}{\tau_i(1-p_i)}\right]^2 + \frac{4p_i}{\tau_i^2(1-p_i)}\right\}^{1/2} \qquad \textbf{[S4]}$$

$$R_{lS} = \frac{1}{2}\left[R_{li} + r_{lo}[CR_o] + R_{lo0} + \tau_i^{-1} + \frac{p_i}{\tau_i(1-p_i)}\right] + \frac{1}{2}\left\{\left[R_{li} - r_{lo}[CR_o] - R_{lo0} + \tau_i^{-1} - \frac{p_i}{\tau_i(1-p_i)}\right]^2 + \frac{4p_i}{\tau_i^2(1-p_i)}\right\}^{1/2} \qquad \textbf{[S5]}$$

$$\frac{a_S}{a_S + a_L} = \frac{1}{2} - \frac{1}{2}\left\{\frac{\left[(R_{li} - r_{lo}[CR_o] - R_{lo0})(1-2p_i) + \frac{p_i}{\tau_i(1-p_i)} + \tau_i^{-1}\right]}{\left\{\left[R_{li} - r_{lo}[CR_o] - R_{lo0} + \tau_i^{-1} - \frac{p_i}{\tau_i(1-p_i)}\right]^2 + \frac{4p_i}{\tau_i^2(1-p_i)}\right\}^{1/2}}\right\} \qquad \textbf{[S6]}$$

R_{1i} and R_{1o0} are the intra- and extracellular ^1H_2O relaxation rate constants in the absence of exchange, and CR_o for the latter. r_{1o} and $[CR_o]$ are the interstitial CR relaxivity and concentration, respectively. p_i and τ_i are the mole fraction and mean lifetime, respectively, of intracellular water molecules. Consider the square root discriminant in Eqs. **S4**–**S6**. When $\tau_i \to \infty$, the NXL (no-exchange-limit), all right-hand side terms with τ_i^{-1} factors vanish. After taking the square root of the square within the discriminant, one chooses the negative root so that $a_S \to (1 - p_i)$, $R_{1S} \to r_{1o}[CR_o] + R_{1o0}$, and $R_{1L} \to R_{1i}$, as they must ($R_{1S} > R_{1L}$).

To complete a DCE-MRI analytical model, such MR observation equations must be combined with a pharmacokinetic rate law describing the interchange of CR molecules between the plasma space, CR_p, and the interstitial space, CR_o. We use the integral rate law (from nuclear medicine) often labeled Kety–Schmidt, also given as Eq. **S7**

$$[CR_o](T) = K^{trans}v_e^{-1}\int_0^T [CR_p](t)e^{-K^{trans}v_e^{-1}(T-t)}dt \qquad \textbf{[S7]}$$

which depends on K^{trans}, the volume fraction rate constant product for CR extra- and intravasation at passive equilibrium, and v_e, the interstitial volume fraction. The Eqs. **1** and **S1**–**S3** matrix forms combined with **S7** produce the second-generation shutter-speed model (SSM2), or BALDERO (Blood Agent Level Dependent and Extravasation Relaxation Overview) (8). The combination of Eqs. **S1**–**S6** with **S7** gives the first-generation SSM (SSM1), or BOLERO (BOLus Enhanced Relaxation Overview) models (2, 9).

The use of the right-hand side of Eq. **2** ($a_L\mathbf{S}_L + a_S\mathbf{S}_S$; identified with the first and second terms of the right-hand side of Eq. **1**, $p'_i\mathbf{S}_i + p'_o\mathbf{S}_o$) is the slow-exchange-regime (SXR)-a BOLERO version (9, 10). The use of only the first right-hand side term of Eq. **2**, $\mathbf{S}_L$ (identified with $\mathbf{S}_i$; $p'_o \to 0$, $a_S \to 0$), which dominates at the beginning of, and often throughout, the DCE-MRI time-course is the fast-exchange-regime (FXR)-a BOLERO version (9, 10).

IR, SR, or Quantitative T_1 acquisitions have allowed clear determinations of situations when $a_S\mathbf{S}_S$ is directly detected—i.e., when the equilibrium intercompartmental water exchange system has been driven to the SXR condition. They facilitate experimental determination of whether, within error, the longitudinal relaxation is mono-exponential [fast-exchange-limit (FXL) or FXR] or bi-exponential [SXR, slow-exchange-limit (SXL), or NXL]. There is distinct evidence that SXR (and even SXL) can be reached in cell suspension systems, and this possibility is reviewed in the next section.

Exchange Domains. Equilibrium water exchange between histological-scale compartments has been studied by NMR for some time. Early work was reviewed almost 20 years ago (11). More recently, clear bi-exponential ^1H_2O relaxation has been reported for in vitro yeast cell suspensions with extracellular relaxation reagent (RR) (ref. 1 and Y. Zhang and J. A. Balschi, personal communication), for in vitro hepatocarcinoma cell pellets with cytosolic RR (12), and for in vivo rat brain with interstitial RR from direct intracerebroventricular infusion (13). Clear bi-exponential relaxation is not observed for human endothelial cells in vitro with cytosolic or endosomic RR (14), for excised, intracellular Mn^{2+}-loaded myocardial tissue after preperfusing rat hearts ex vivo with modest concentrations of $MnCl_2$ (15), for rat thigh muscle in vivo at steady-state extracellular RR perfusion (2, 7), and for human brain in vivo during the first pass (16) and during the wash-out (17) after intravascular bolus RR injection. Each of these latter reports (2, 7, 14–17), however, presents strong evidence for the departure from the FXL for the FXR condition. One can also use extracellular flow relaxivity (18) to raise longitudinal r^{-1} sufficiently that the equilibrium transcytolemmal water-exchange system reaches even the SXL for microbead-attached HeLa cell pellets (19).

Calibration Curves. Some sample putative calibration curves implicit in the DCE-MRI pharmacokinetic analyses are shown in supporting information (SI) Fig. S1 as plots of signal intensity (S) versus interstitial CR concentration ($[CR_o]$) (not the time axis of Fig. 1 in the text). Parameter values for these particular curves are given in the legend. Some quantities for Fig. S1 *a–c* are: $v_e = 0.4$ ($p_o = v_e/f_W = 0.5$), $r_{1o} = 4.1\ s^{-1}{\cdot}mM^{-1}$, $R_{10} = 0.83\ s^{-1}$, and $R_{1i} = R_{1o0}$. These would be governed by nature (v_e) and also by the physiological temperature and the magnetic field strength used (r_1 and R_1 parameters). The curves also depend on τ_i, which is determined by nature and the physiological temperature. Six curves are calculated for each panel by using Eqs. **S1–S6**. The upper dotted (purple) curve results when $\tau_i \to 0$ and is labeled FXL. The lower dotted curves result when $\tau_i \to \infty$ and are labeled NXL (red and blue for the SXR-a and FXR-a versions, respectively). Three Shutter-Speed Model curves are calculated with $\tau_i = 370$ ms: $a_L\mathbf{S}_L + a_S\mathbf{S}_S$ (SXR-a, black solid curve), $a_S\mathbf{S}_S$ (SXR-a, black dashed curve), and $\mathbf{S}_L$ (FXR-a, blue solid curve). It makes sense that the SXR-a (black) and FXR-a (blue) traces are always between their respective FXL and NXL limiting curves. In Fig. S1*d*, $v_e = 0.65$, and $\tau_i = 400$ ms for the black and blue solid curves.

Of course, during a data-fitting procedure, the computer program is incrementing the variable parameters. Because, for the work here, this always involves varying v_e, and sometimes also τ_i, these (implicit) calibrations are different for each incrementation.

These curves are independent of the K^{trans} value, which is determined by the integrated time-course and extent of the $[CR_o]$ excursion from left to right and back during the bolus passage. As we have described before (10), the exchange system always starts in the FXL condition, and it enters the FXR condition where the FXR-a (blue) curve departs from the FXL curve (purple dotted), ≈0.14 mM in panel a. If the $[CR_o]$ value proceeds past where the SXR-a (black) curve departs from the FXR-a (blue) curve (≈0.3 mM in *a*), the system has entered the SXR condition. The system passes back through these exchange conditions to the FXL as CR washes out of the tissue. The Fig. S1 curves also depend on the pulse sequence parameters, TR and α, which are under operator control. For Fig. S1 *a–d*, these are 10, 10, 4, and 10 ms, and 10°, 30°, 10°, 30°, respectively. It is clear that the pulse sequence parameters affect the exchange sensitivity (dynamic range between the dotted curves) and the signal strength: the ordinate is the same for each panel.

It is important to note that the Fig. S1 curves are constructed for unit transverse relaxation E_2^* factors (Eq. **S3**), i.e., as if TE = 0. Even so, the maximum fractional $a_S\mathbf{S}_S$ contribution—reached at $[CR_o]_{max}$—never becomes very large. For benign and malignant lesions, $[CR_o]_{max}$ is typically 0.5 and 1.6 mM, respectively (20). For Fig. S1*a*, $[a_S\mathbf{S}_S/(a_L\mathbf{S}_L + a_S\mathbf{S}_S)]$ is 0.05 and 0.29 at these two $[CR_o]_{max}$ values (Fig. S1*a* was extrapolated for the latter).

The general closeness of the red dotted and black solid Fig. S1 curves suggests that there will not be large parameter value differences when data are analyzed with the FXL-c (SM) and SXR-a (SSM) models. The IDC/DCIS results in Table 1 bear this out. Although the v_e value is increased by 31%, the K^{trans} value is increased not at all. As $[CR_o]$ builds, the opposite signs between identical terms on the right-hand sides of Eqs. **S4** and **S5** mean that the $a_S\mathbf{S}_S$ term begins to partially nullify the $a_L\mathbf{S}_L$ term on the right-hand side of Eq. **2**. This dilutes the latter's nonlinear $[CR_o]$ dependence. This is not a problem when the $a_L\mathbf{S}_L$ and $a_S\mathbf{S}_S$ terms can be discriminated (the SXR) and individually fitted (as R_{1L} and R_{1S}) (1).

These curves also suggest why analysis using SXR-a might return a very much larger τ_i value than would analysis using FXR-a. Assume that an actual situation is best represented by the FXR-a blue curve, in Fig. S1*b* for example—that is, the $a_S\mathbf{S}_S$ term contribution is truly negligible, for some reason. But, in each iteration the data are analyzed with the SXR-a model, which uses the black curve. A way for the black curve to mimic the behavior of the blue curve is to have a τ_i value larger than that of the latter (370 ms). However, the black curve cannot go below its red dotted NXL lower limit. Thus, the τ_i value returned is pegged at the largest value allowed in the computer algorithm. For the data in the main text, this result occurs for 86% of the malignant tumors and for 73% of the benign lesions. An analogous situation may obtain for equilibrium transendothelial water exchange (21). Simulations confirm that SXR-a analysis of data generated with only $\mathbf{S}_L$ underestimates K^{trans} and v_e, and overestimates τ_i.

Literature Comparison. It is important to compare the parameter values determined from DCE-MRI pharmacokinetic analyses with independent measures of the same quantities. In general, we find that the FXR-a version of the SSM yields results in quite good agreement with the literature. This usually means that the Standard Model (FXL-c) parameter values do not agree as well. Also, the breast tumor findings presented in this paper suggest that there may be situations where the SXR-a Shutter-Speed version also yields results that include systematic error. The following are surveys for the three parameters often varied in FXR-a SSM analyses.

K^{trans}. The K^{trans} parameter is usually the most precisely determined (Table 1). It is the most sensitive to the initial slope of the DCE-MRI signal time-course. We are not aware of gold standard K^{trans} measurements for exact CR analogs in solid tumors such as in the breast. At sufficiently high magnetic field, however, CR detectability is sufficiently increased (22) to measure CR extravasation in even normal human brain, where a comparison is available. Thus, an FXR-a (SSM) analysis yields a K^{trans} value of 2.9×10^{-5} min^{-1} for the Gd(HP-DO3A) CR in normal white matter (23), in good agreement with gold standard, sacrificial autoradiographic analyses of rodent brain data obtained (at the earth's magnetic field) with radiotracers almost chemically identical to the MRI CR (24, 25). However, an FXL-constrained (SM) analysis of the same normal white matter MRI data (23) increases K^{trans} to 4.5×10^{-5} min^{-1} and out of agreement with the tracer results. In this case, the SM raises K^{trans} because the pertinent exchange is equilibrium trans*endothelial* water interchange. Careful analyses of these brain DCE-MRI data demonstrate that the SXR condition is never reached, even during the CR first pass, albeit at half the standard dose (16).

v_e. The v_e values in several different normal muscle tissues *in vivo* obtained by analyses of DCE-MRI pharmacokinetic data with the FXR-a SSM have been surveyed: the range is 0.09 − 0.2 (table 1 of ref. 26). These are in good agreement with classical determinations (26). The malignant tumor v_e values returned by FXR-a SSM (9, 26–31) can sometimes be quite large. However, some time ago, Gullino reported neoplastic solid tumor v_e values to be "very large," ranging from 0.2 to 0.5 as determined by classic radioisotope dilution measurements (32). Note, that except for one malignant tumor [that is mostly benign tissue (33)], here it is *benign* lesions that have the larger Fig. 2*B* SSM v_e values. In fact, the mean FXR-a v_e value for all seven malignant tumors is 0.59 (Fig. 2*B*), at the edge of Gullino's range. Thus, the malignant lesion v_e values we report are in rather good agreement with Gullino's survey. In most cases, v_e may be related to the tissue "cellularity" complement. It is possible, however, that in some very advanced tumors there are regions with significant necrosis and/or cell cytolemmae so compromised that CR enters even the cells. It is also possible that CR enters some mammary duct lumen regions (34). In cases such as these, the v_e parameter is better thought of as an effective CR distribution volume fraction, v_D, and not attributed to exclusively interstitial space. Perhaps a number of the benign lesions here are cyst-like.

We suspect, however, that the very large v_e values of some benign lesions may be overestimates (i.e., more than just imprecise). The CR uptake in most benign tumors is very slow, reflecting the fact that K^{trans} is small (Fig. 2*A*). Thus, the rise in signal intensity is sufficiently slow that the maximum is usually not reached before DCE-MRI acquisition ceases (Fig. 1*D*), and thus the time-course curve is never completely defined. Because v_e is most sensitive to the area under the DCE-MRI time-course, it may suffer particularly from this premature pharmacokinetic acquisition period truncation.

Fig. S1*d*, with the large v_e of 0.65, exhibits unusual curves. As stated above, however, we find v_e values this large for almost exclusively benign tumors. Besides the fact that a larger v_e requires more CR to reach a given $[CR_o]$, all of these tumors have small K^{trans} values. Thus, the rate of entry of CR into the interstitium is slow, and $[CR_o]$ does not have a chance to rise very far before wash-out takes over. Rightward excursion on the abscissa of Fig. S1*d* would seem to be self-limited, and may never significantly reach the SXR. If $p_o > 0.5$ (as in *d*), then at sufficiently large $[CR_o]$ a_S will become larger than a_L. When $a_S = p_o$, the SXL has been reached (7).

In a DCE-MRI study of murine implanted RIF-1 tumors, it was found that FXL-c (SM) analyses yielded tumor rim v_e values that decreased significantly with increasing CR dose (27). Of course, the v_e value is defined to be a tumor tissue property and should not be dependent on the CR dose or rate of delivery. We had previously shown with first-principle theory and simulation that the assumption of effectively infinitely fast equilibrium transcytolemmal water exchange by the FXL-c model would be manifest as precisely such CR dose dependence (9). Application of FXR-a (SSM) analyses to the same data eliminated most of the CR dose dependence and yielded constant v_e values at ≈0.65 (27). Thus, when not CR dose-quenched, the SM also returns large tumor v_e values. Such dose dependence may contribute to literature SM irreproducibility.

τ_i. Often the least precisely determined of the three parameters usually varied in FXR-a DCE-MRI analyses is τ_i (9). However, a number of recent such studies have reported τ_i values consistently ranging from a few tenths of second to a few seconds, for a wide variety of normal and pathological tissues (9, 26–30, 35). These values are in excellent agreement with what one calculates from classic "gold standard" physiology. For a spherical cell, "well-mixed" theory gives: $\tau_i = r/(3P_W)$, where r is the cell radius, and P_W is the cytolemmal water permeability coefficient (1). Taking a "typical" spherical parenchymal cell of $r = 5$ μm to have $P_W = 1.4 \times 10^{-4}$ cm/s (36) gives a value for τ_i of 1.2 s.

Furthermore, several recent NMR studies used rigorous Quantitative T_1 family acquisitions to yield much more well-determined τ_i values (refs. 1, 7, 12–15, and 19 and Y. Zhang and J. A. Balschi, personal communication), which nonetheless fall in the same range as the DCE-MRI experiments. Because cytolemmal water permeability, and thus P_W, surely has an active component sensitive to cellular metabolic state (Y. Zhang and J. A. Balschi, personal communication), τ_i is surely a desirable DCE-MRI biomarker. It is especially sensitive to the shape of the DCE-MRI signal time-course (9).

Interstitial Field Inhomogeneities. When a paramagnetic CR is constrained to a vessel lumen, there are significant magnetic field inhomogeneities in the perivascular space (37). This is visualized, for example, as the "blooming" around large cerebral vessels in contrast-enhanced susceptibility-weighted images (38). At the small (2, 37) peak $[CR_b]$ value of 2.5 mM after the standard dose monomeric Gd(III) chelate bolus injection (Fig. 1*D Inset*), the blood susceptibility is −8.3 ppm (37, 39). We can use magnetic susceptibility first principles to calculate the magnetic field dispersion just outside the surface of a vessel oriented perpendicular to the main magnetic field to be 0.8 ppm (0.4 to −0.4), and at a distance of even one vessel radius from the surface to be 0.6 ppm (0.3 to −0.3) (37, 39). As shown in the main text, this could cause significant "quenching" of the signal from spins in these regions in a clinical DCE-MRI acquisition.

Then, as CR enters the interstitium the susceptibility of the entire interstitium increases, and the difference between that and the cytoplasmic value causes field inhomogeneities that are larger in interstitial spaces. This is predicted by susceptibility first principles (37) and confirmed by MR spectroscopy. In vivo $^{23}Na_o$ spectral lines are considerably broader than $^{23}Na_i$ peaks in the presence of interstitial $DyTTHA^{3-}$ (40, 41), and this broadening is caused by susceptibility gradients (40). These peaks are discriminated because transcytolemmal Na^+ exchange is quite slow. Because relative susceptibility broadening is independent of the resonant nucleus (37),

the same greater broadening (in ppm) will affect the unresolvable interstitial ^1H_2O resonance. Because the ^1H resonant frequency is approximately 4 times that of ^{23}Na, the absolute inhomogeneous broadening will be significantly greater for ^1H.

Perhaps all of these geometric susceptibility aspects are exacerbated for the abnormal, convoluted neoplastic tumor capillary bed morphology (42).

1. Labadie C, Lee J-H, Vétek G, Springer CS (1994) Relaxographic imaging. *J Magn Reson B* 105:99–112.
2. Landis CS, *et al.* (2000) Determination of the MRI contrast agent concentration time course *in vivo* following bolus injection: Effect of equilibrium transcytolemmal water exchange. *Magn Reson Med* 44:563–574.
3. Look DC, Locker DR (1970) Time saving in measurement of NMR and EPR relaxation times. *Rev Sci Instr* 41:250–251.
4. Kaptein R, Dijkstra, Tarr CE (1976) A single-scan Fourier transform method for measuring spin-lattice relaxation times. *J Magn Reson* 24:295–300.
5. Grinstead JW, Rooney WD (2008) Fast T_1 mapping in human brain using inversion recovery EPI with GRAPPA at 3T and 7T. *Proc Int Soc Magn Reson Med* 16:3084.
6. Woessner DE (1961) Nuclear transfer effects in nuclear magnetic resonance pulse experiments. *J Chem Phys* 35:41–48.
7. Landis CS, *et al.* (1999) Equilibrium transcytolemmal water-exchange kinetics in skeletal muscle *in vivo. Magn Reson Med* 42:467–478.
8. Li X, Rooney WD, Springer CS (2005) A unified magnetic resonance imaging pharmacokinetic theory: Intravascular and extracellular contrast reagents. *Magn Reson Med* 54:1351–1359, and erratum (2006) 55:1217.
9. Yankeelov TE, Rooney WD, Li X, Springer CS (2003) Variation of the relaxographic ''shutter-speed'' for transcytolemmal water exchange affects the CR bolus-tracking curve shape. *Magn Reson Med* 50:1151–1169.
10. Springer CS, Yankeelov TE, Li X, Rooney WD, Medina DC (2004) Longitudinal relaxographic NMR ''shutter-speed'' for equilibrium transcytolemmal water exchange varies with interstitial CR level. *Proc Int Soc Magn Reson Med* 12:1969.
11. Hills BP, Belton PS (1989) NMR studies of membrane transport. *Ann Rep NMR Spectrosc* 21:99–159.
12. Terreno E, *et al.* (2006) Effect of the intracellular localization of a Gd-based imaging probe on the relaxation enhancement of water protons. *Magn Reson Med* 55:491–497.
13. Quirk JD, *et al.* (2003) Equilibrium water exchange between the intra- and extracellular spaces of mammalian brain. *Magn Reson Med* 50:493–499.
14. Strijkers GJ, Hak S, Kok MB, Springer CS, Nicolay K (2008) A three-compartment T_1-relaxation model for intracellular contrast agents: Implications for molecular MR imaging. *Proc Int Soc Magn Reson Med* 16:18.
15. Seland JG, Bruvold M, Brurok H, Jynge P, Krane J (2007) Analyzing equilibrium water exchange between myocardial tissue compartments using dynamical two-dimensional correlation experiments combined with manganese-enhanced relaxography. *Magn Reson Med* 58:674–686.
16. Rooney WD, *et al.* (2004) First pass bolus-tracking measurement of transendothelial water exchange in healthy controls. *Proc Int Soc Magn Reson Med* 12:1390.
17. Rooney WD, Yankeelov TE, Coyle PK, Telang FW, Springer CS (2003) Regional blood volumes and intravascular water lifetimes in human brain. *Proc Int Soc Magn Reson Med* 11:2188.
18. Lee J-H, Li X, Sammi MK, Springer CS (1999) Using flow relaxography to elucidate flow relaxivity. *J Magn Reson* 136:102–113.
19. Zhao L, *et al.* (2008) Intracellular water-specific MR of microbead-adherent cells: The HeLa cell intracellular water exchange lifetime. *NMR Biomed* 21:159–164.
20. Springer CS, *et al*. (2008) Molecular aspects of NMR shutter-speed discrimination of malignant and benign breast tumors. *Proc Int Soc Magn Reson Med* 16:3830.
21. Li X, Springer CS, Jerosch-Herold M (2008) First-pass DCR-MRI with extravasating CR: Evidence for human myocardial capillary recruitment in adenosine-induced hyperemia. *NMR Biomed*, 10.1002/nbm.1293.
22. Rooney WD, *et al*. (2007) Magnetic field and tissue dependencies of human brain longitudinal ^1H_2O relaxation *in vivo. Magn Reson Med* 57:308–318.
23. Rooney WD, Telang FW, Springer CS (2002) Quantitative 4T determination of normal human brain vascular properties suggests CR transport across BBB. *Proc Int Soc Magn Reson Med* 10:1314.
24. Blasberg RG, Fenstermacher JD, Patlak CS (1983) Transport of α-aminoisobutyric acid across brain capillary and cellular membranes. *J Cereb Blood Flow Metabol* 3:8–32.
25. Preston E, Foster DO (1993) Diffusion into rat brain of contrast and shift reagents for magnetic resonance imaging and spectroscopy. *NMR Biomed* 6:339–344.
26. Yankeelov TE, *et al.* (2005) Evidence for shutter-speed variation in CR bolus-tracking studies of human pathology. *NMR Biomed* 18:173–185.
27. Zhou R, Pickup S, Yankeelov TE, Springer CS, Glickson JD (2004) Simultaneous measurement of arterial input function and tumor pharmacokinetics in mice by dynamic contrast enhanced imaging: Effects of transcytolemmal water exchange. *Magn Reson Med* 52:248–257.
28. Li X, *et al.* (2005) Shutter-speed analysis of contrast reagent bolus-tracking data: Preliminary observations in benign and malignant breast disease. *Magn Reson Med* 53:724–729.
29. Chang EY, *et al.* (2008) The evaluation of esophageal adenocarcinoma using dynamic contrast enhanced magnetic resonance imaging. *J Gastrointestinal Surg* 12:166–175.
30. Kim, *et al*. (2007) Transcytolemmal water exchange in pharmacokinetic analysis of dynamic contrast-enhanced MRI data in squamous cell carcinoma of the head and neck. *J Magn Reson Imaging* 26:1607–1617.
31. Yankeelov TE, Luci JJ, DeBusk LM, Lin C, Gore JC (2008) Incorporating the effects of transcytolemmal water exchange in a reference region model for DCR-MRI analysis: Theory, simulations, and experimental results. *Magn Reson Med* 59:326–335.
32. Gullino PM (1975) Extracellular compartments of solid tumors. *Cancer: A Comprehensive Treatise*, ed Becker FF (Plenum, New York), Vol 3, p 341.
33. Huang W, *et al.* (2008) The MR shutter speed discriminates vascular properties of malignant and benign breast tumors *in vivo. Proc Natl Acad Sci USA*, 10.1073/PNAS.0711226105.
34. Jansen SA, *et al*. (2008) Why do ductal carcinoma in situ lesions enhance on dynamic contrast enhanced MRI of the breast? Using X-ray fluorescence and MRI to track the spatial distribution of Gd-DTPA in murine DCIS. *Proc Int Soc Magn Reson Med* 16:365.
35. Yankeelov, *et al*. (2007) Integration of quantitative DCE-MRI and ADC mapping to monitor treatment response in human breast cancer: Initial results. *Magn Reson Imaging* 25:1–13.
36. House CR (1974) *Water Transport in Cells and Tissues* (Edward Arnold, London), p 156.
37. Springer CS (1994) Physicochemical principles influencing magnetopharmaceuticals. *NMR in Physiology and Biomedicine*, ed Gillies RJ (Academic, San Diego), pp 75–99.
38. Sehgal V, *et al*. (2006) Susceptibility-weighted imaging to visualize blood products and improve tumor contrast in the study of brain masses. *J Magn Reson Imaging* 24:41–51.
39. Albert MS, Huang W, Lee J-H, Patlak CS, Springer CS (1993) Susceptibility changes following bolus injections. *Magn Reson Med* 29:700–708.
40. Balschi JA, Kohler SJ, Bittl JA, Springer CS, Ingwall JS (1989) Magnetic field dependence of ^{23}Na NMR spectra of rat skeletal muscle infused with shift reagent *in vivo. J Magn Reson* 83:138–145.
41. Balschi JA, Bittl JA, Springer CS, Ingwall JS (1990) ^{31}P and ^{23}Na NMR spectroscopy of normal and ischemic rat skeletal muscle. Use of a shift reagent *in vivo. NMR Biomed* 3:47–58.
42. Jain RK (2005) Normalization of tumor vasculature: An emerging concept in antiangiogenic therapy. *Science* 307:58–62.

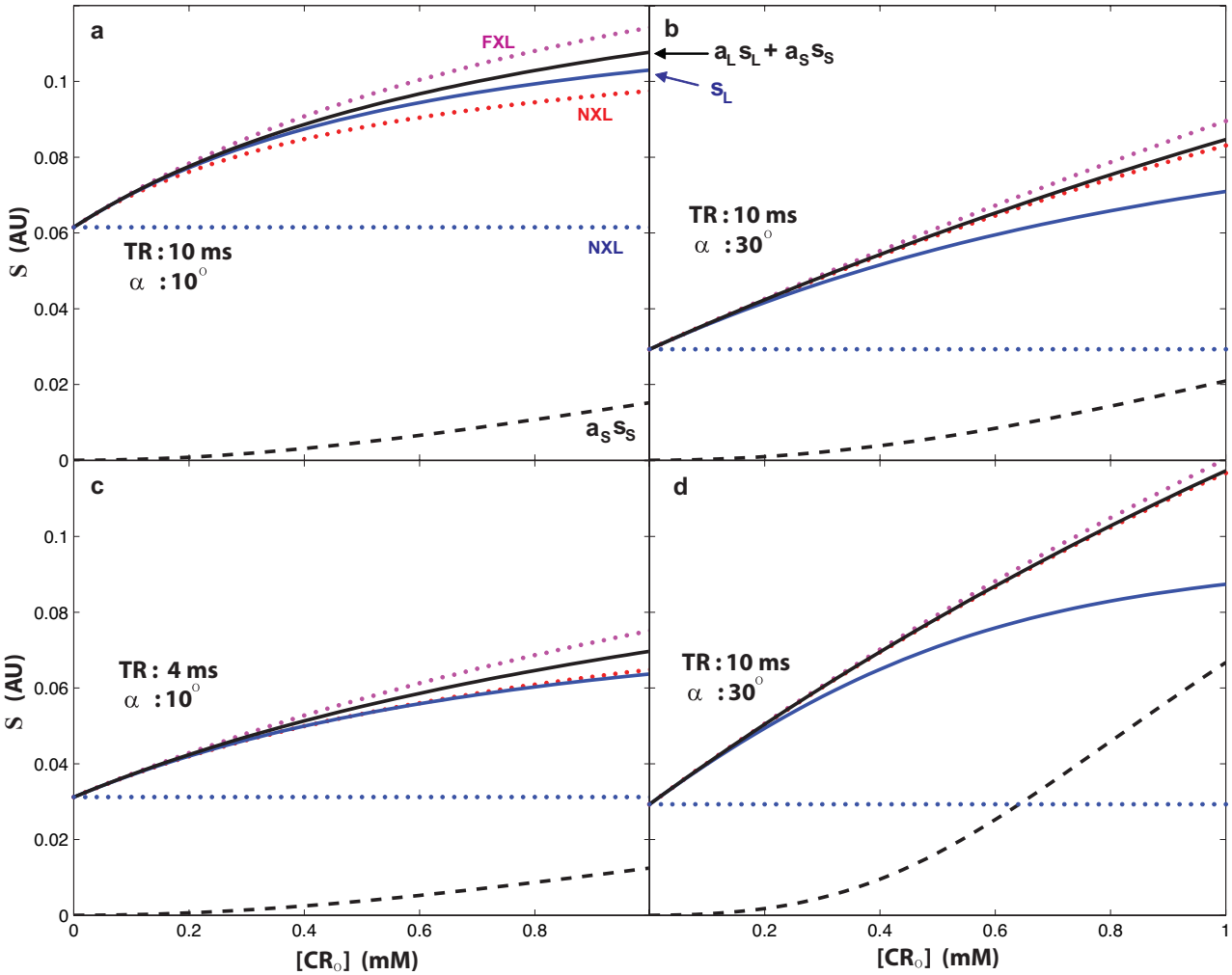

Fig. S1. Putative calibration curves implicit in the pharmacokinetic analyses. These are plots of ^1H_2O signal intensity (S) versus the interstitial concentration of contrast reagent, [CR_o]. Parameter values for these calculations are $r_{1o} = 4.1\ s^{-1}{\cdot}mM^{-1}$, $R_{10} = 0.83\ s^{-1}$, and $R_{1i} = R_{1o0}$. For *a*, *b*, and *c*, $v_e = 0.40$ ($p_o = v_e/f_W = 0.50$) and $\tau_i = 370$ ms. For *d*, $v_e = 0.65$ ($p_o = v_e/f_W = 0.81$) and $\tau_i = 400$ ms. The values of TR and α are given in each panel. The black and blue solid and black dashed curves are plots of the labeled terms and factors of (main text) Eq. **2**. The red and blue dotted curves have meanings analogous to those of (main text) Fig. 1.